Sharpening Fibers in Diffusion Weighted MRI via Erosion

Thomas C.J. Dela Haije, Remco Duits, and Chantal M.W. Tax

Abstract In this chapter erosion is generalized to the space of diffusion weighted MRI data. This is done effectively by solving a Hamilton-Jacobi-Bellman (HJB) system (erosion) on the coupled space of three dimensional positions and orientations, embedded as a quotient in the group of three dimensional rigid body motions. The solution to the HJB equations is given by a well-posed morphological convolution. We present two numerical approaches to solve the HJB equations: analytical kernels, and finite differences. Proof of concept is given by showing improved visibility of major fiber bundles in both artificial and human data. Furthermore, the method is shown to significantly improve the output of a probabilistic tractography algorithm used to extract the optic radiation.

Keywords Diffusion weighted MRI • Erosion • Hamilton-Jacobi-Bellman equations • Lie groups • Regularization • Sharpening • Sub-Riemannian • Geometry

1 Introduction

Diffusion Weighted MRI (DW-MRI) is a collection of magnetic resonance imaging techniques used to infer structural information from fibrous tissue such as the brain white matter. DW-MRI locally measures diffusion [46], the random motion of molecules, in one or multiple directions. Because this motion is less constrained along the fiber direction than across, these measurements effectively characterize

T.C.J. Dela Haije (✉) • R. Duits
Imaging Science and Technology Eindhoven (IST/e), Eindhoven University of Technology, Eindhoven, The Netherlands
e-mail: T.C.J.Dela.Haije@tue.nl,R.Duits@tue.nl

C.M.W. Tax
Image Sciences Institute (ISI), University Medical Center Utrecht, Utrecht, The Netherlands
e-mail: chantal@isi.uu.nl

C.-F. Westin et al. (eds.), *Visualization and Processing of Tensors and Higher Order Descriptors for Multi-Valued Data*, Mathematics and Visualization,
DOI 10.1007/978-3-642-54301-2_5,

tissue orientation. A prevalent means to analyze this data is tractography, which tries to join locally registered fiber fragments based on their alignment, producing fiber tracts that potentially represent nerve bundles. A simpler application of DW-MRI is for instance the diagnosis and assessment of stroke, where swelling of the cells appears to hinder diffusion significantly [51].

1.1 Diffusion Weighted MRI

Interpretation of the diffusion measurements is an area of active research. A variety of models have been suggested to extract diffusion features, the most common of which is Diffusion Tensor Imaging (DTI) [2, 4, 34, 36]. In DTI, the measured diffusion in a number of directions $\mathbf{n} \in S^2$ after a time t is assumed to satisfy an anisotropic Gaussian distribution. The space S^2 is the ordinary sphere given by the collection of $\mathbf{x} \in \mathbb{R}^3$ that satisfy $\|\mathbf{x}\| = 1$. A symmetric, second order, three-dimension tensor $D(\mathbf{x})$ is estimated at each spatial point $\mathbf{x} \in \mathbb{R}^3$, such that the local amount of diffusion $p(\mathbf{n}|\mathbf{x})$ in the direction $\mathbf{n}$ is given by [1]

$$p(\mathbf{n}|\mathbf{x}) = \frac{1}{2\pi t^{\frac{3}{2}}\sqrt{|\det D(\mathbf{x})|}} \left(\frac{\mathbf{n}^T (D(\mathbf{x}))^{-1} \mathbf{n}}{t} \right)^{-\frac{3}{2}}. \tag{1}$$

More complicated models such as the diffusion orientation transform [39] use more measurements to reconstruct this $p(\mathbf{n}|\mathbf{x})$, called the Orientation Distribution Function (ODF), with fewer model assumptions [28].

From the measured ODF, which gives the diffusion likelihood in a certain direction *given* a position, we find the likelihood at any combination $(\mathbf{x}, \mathbf{n})$ from

$$p(\mathbf{x}, \mathbf{n}) = p(\mathbf{n}|\mathbf{x})\, p(\mathbf{x}), \tag{2}$$

where $p(\mathbf{x})$ is an a priori distribution on position space only, and $(\mathbf{x}, \mathbf{n}) \mapsto p(\mathbf{x}, \mathbf{n})$ is a spatial distribution of diffusivity profiles. A typical function description of $p(\mathbf{x})$ would be the normalized indicator function $p(\mathbf{x}) = \frac{1_\Omega(\mathbf{x})}{\mu_\Omega}$, where $\Omega \subset \mathbb{R}^3$ is the region of the brain that contains the white matter, and μ is the measure.

Diffusivity profiles are typically visualized by morphed spheres called glyphs. The diffusion likelihood $p(\mathbf{x}, \mathbf{n})$ determines the radius of the sphere at $\mathbf{x}$ in the direction $\mathbf{n}$.

1.2 Enhancement and Tractography

While DW-MRI is unique in its ability to measure the microstructure of the brain in vivo, it has some notable drawbacks. The scanning time, primarily determined by

the number of directions needed to reliably fit a certain model, can be in the order of hours for the more complex scanning protocols [52]. Decreasing the number of scanning directions generally decreases the reliability of a fit. Secondly, the scanning time is usually minimized by utilizing very fast imaging sequences such as the echo-planar imaging sequence. These invariably result in noisy data, resulting in a less reliable signal.

The consequences of this are apparent. While the obtained glyphs will still generally point in the directions of the major fiber bundles at each point, simply looking at the local maximum likelihoods is often not enough to reliably determine these directions. Following the emergence of the tractography methods that are based on these directions, the importance of enhancement techniques in neurological applications pertaining to tractography grew [7–9, 40, 47–49].

1.3 Sharpening

Difficulties still remain though, as enhancement inadvertently lowers the level of detail and contrast. To remedy this, one typically uses sharpening methods that emphasize prominent features by attempting to increase contrast at interesting points in the data, typically edges. Previous attempts to sharpen DW-MRI data sets [16, 25, 26, 29, 38] have primarily focused on angular sharpening, i.e. the sharpening of each glyph individually. Promising results have been obtained, but by only considering angular sharpening one by definition ignores the available spatio-angular information. Secondly, many of the proposed methods are based on deconvolution, a process which is in principle ill-posed.

In this article we outline a well-posed alternative based on grayscale morphology, extending well established works [6, 50, 53] on $\mathbb{R}^3$ to the space of diffusion images. By defining an erosion operator for DW-MRI we can slim fibrous structures in the spatial and the angular domain simultaneously. To improve reliability, we take into account the context: if a glyph and its neighbors are aligned, then the likelihood that the direction of alignment is equal to the direction of the nervous fiber bundle is increased. This is illustrated in Fig. 1. Contextual processes have previously been shown to be useful in enhancements [13, 18, 20, 41–43].

Our framework relates to the general framework of group morphology [44] applied to the group of three dimensional rigid body motions $SE(3)$. In addition to Roerdink [44] we rely on scale-space PDE's whose solutions are given by a morphological convolution with the corresponding Green's function. Furthermore, we extend the morphological group convolutions on $SE(3)$ to morphological convolutions on the quotient $SE(3)/(\{\mathbf{0}\} \times SO(2))$, see Sect. 3.3.1.

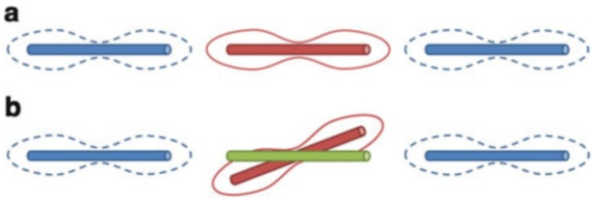

Fig. 1 If we take into account only the local diffusivity profiles, then both of the orientations indicated by the *red bars* would be considered equally correct (**a**). If we take into account the context however, here illustrated by the *blue glyphs*, we will see that in (**b**) the orientation given by the *green bar* seems more likely to be correct than the *red* one. This information can be exploited to improve the results of contextual operators

1.4 Outline of the Article

The article is structured as follows. Section 2 presents a summary of previously published theory, which is used in Sect. 3 to define the erosion operator used to sharpen the DW-MRI data. This section also covers implementation issues. Some practical uses of the erosion operator are lastly given in Sect. 4.

2 Interpreting the Data

We will consider the diffusion images as (twice differentiable) functions on the space of positions and orientations $\mathbb{R}^3 \times S^2$, i.e. $U \in C^2(\mathbb{R}^3 \times S^2, \mathbb{R}^+)$, where $U(\mathbf{x}, \mathbf{n}) = p(\mathbf{x}, \mathbf{n})$ as defined in Eq. (2). To grasp the structure of this space, we must realize that the spaces of positions and orientations are coupled. This can be argued from the concept of alignment, which is impossible to define on the decoupled space, as demonstrated in Fig. 2.

In this section we will show that by embedding the space $\mathbb{R}^3 \times S^2$ as a quotient in the special Euclidean group, we can not only make this idea of a coupled space concrete, but we can also impose in a straightforward way operator invariance under rotations and translations. Once we have clarified the natural group structure embodying $\mathbb{R}^3 \times S^2$, we continue by defining the Euclidean-invariant moving frame of reference and the accompanying legal metrics. These metrics will be used in the next section as the basis for the erosion process. To keep the length of the article at bay, many of the details and proofs are omitted. A more extensive overview of the theory is available [20].

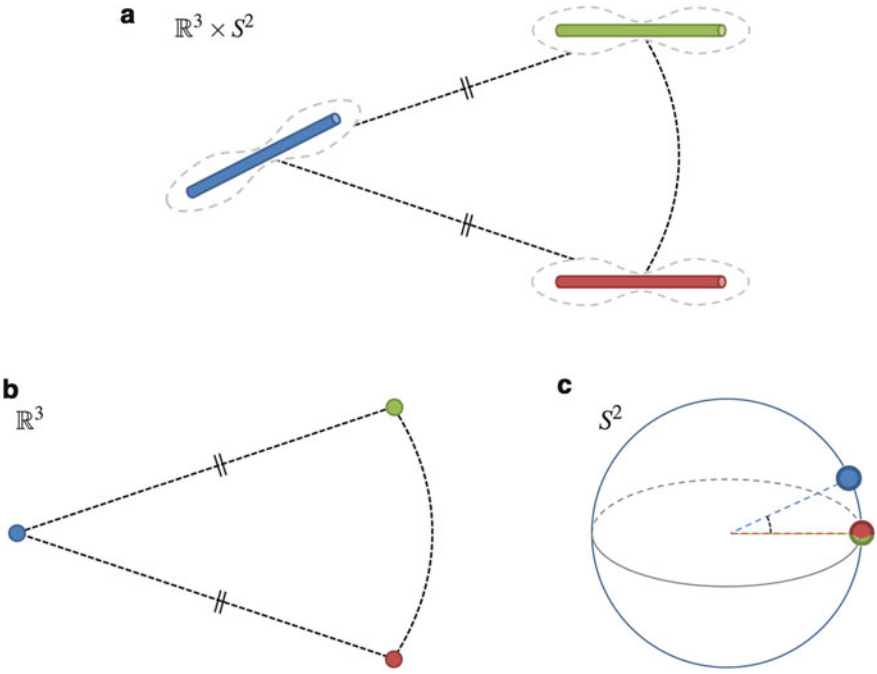

Fig. 2 An illustration in the space $\mathbb{R}^3 \times S^2$ of the coupled nature of alignment. The situation sketched in (**a**) shows three glyphs and their main directions, with the *blue* and the *green glyphs* visually more aligned than the *blue* and the *red glyphs*. The bars that indicate the main directions are elements of the space of positions and orientations $\mathbb{R}^3 \times S^2$. If we now consider projections onto the subspaces $\mathbb{R}^3$ and S^2 *separately* (**b** and **c** respectively) as we do when we consider $\mathbb{R}^3 \times S^2$ as a Cartesian space, we see that we lose the ability to distinguish between the *green* and the *red bars*. This is essentially due to the fact that the spatial and angular distances between the *blue* and the *green bar* are equal to the respective spatial and angular distances between the *blue* and the *red bar*

2.1 The Group Structure and Euclidean-Invariance

As stated above, the manner in which to define this elusive coupling follows naturally from the embedding of $\mathbb{R}^3 \times S^2$ into the special Euclidean group $SE(3)$ of three-dimensional translations and rotations. Elements of $SE(3) = \mathbb{R}^3 \rtimes SO(3)$ are of the form $(\mathbf{x}, Q)$, and the set is endowed with the group operation

$$(\mathbf{x}, Q)(\mathbf{x}', Q') = (Q.\mathbf{x}' + \mathbf{x}, Q.Q').$$

The group of 3D rigid body motion is commonly denoted by $SE(3)$. Intuitively, the group product represents the fact that a concatenation of two rigid body motions ($(\mathbf{x}, Q)$ and $(\mathbf{x}', Q')$) is again a rigid body motion with translation vector $Q.\mathbf{x}' + \mathbf{x}$

and rotation matrix QQ'. The Special Euclidean motion group is the semi-direct product $\mathbb{R}^3 \rtimes SO(3)$ of the translation group $\mathbb{R}^3$ and rotation group $SO(3)$. This is not a direct product as the rotation part affects the product in the position part. Therefore one writes $SE(3) = \mathbb{R}^3 \rtimes SO(3)$ instead of $\mathbb{R}^3 \times SO(3)$. As we will see next, this semi-direct product structure is responsible for a coupling between spatial and angular space, in the space $\mathbb{R}^3 \rtimes S^2$ embedded in $SE(3)$.

The embedding is realized by identifying the elements of $\mathbb{R}^3 \times S^2$ with the elements of $SE(3)$. We do this by defining the intermediary space

$$\mathbb{R}^3 \rtimes S^2 := SE(3)/(\{\mathbf{0}\} \times SO(2)),$$

where we identify $SO(2)$ with rotations around the vector $\mathbf{e}_z$. As a result, elements of $\mathbb{R}^3 \rtimes S^2$ are equivalence classes of $SE(3)$ under the equivalence relation

$$(\mathbf{x}, Q) \sim (\mathbf{x}', Q') \Leftrightarrow \left(\mathbf{x} = \mathbf{x}' \text{ and } \exists_{\alpha \in [0,2\pi)} Q = Q'.Q_{\mathbf{e}_z,\alpha}\right), \tag{3}$$

with $Q_{\mathbf{e}_z,\alpha}$ a rotation by angle α around $\mathbf{e}_z$. Each equivalence class $[(\mathbf{x}, Q)] = \{(\mathbf{x}', Q') \in SE(3) | (\mathbf{x}', Q') \sim (\mathbf{x}, Q)\}$ can be uniquely identified with an element of $\mathbb{R}^3 \times S^2$, using the relation

$$\mathbb{R}^3 \rtimes S^2 \ni [(\mathbf{x}, Q_{\mathbf{n}})] \Longleftrightarrow (\mathbf{x}, \mathbf{n}) \in \mathbb{R}^3 \times S^2, \tag{4}$$

where $Q_{\mathbf{n}}.\mathbf{e}_z \equiv \mathbf{n}$. The explicit relation between elements of $SE(3)$ and $\mathbb{R}^3 \rtimes S^2$ is then given by

$$SE(3) \ni (\mathbf{x}, Q) \longleftrightarrow [(\mathbf{x}, Q)] \in \mathbb{R}^3 \rtimes S^2, \tag{5}$$

where it should be noted that any two distinct elements $(\mathbf{x}, Q_{\mathbf{n}}), (\mathbf{x}', Q'_{\mathbf{n}}) \in [(\mathbf{x}, Q_{\mathbf{n}})]$ are both mapped to the same equivalence class $[(\mathbf{x}, Q_{\mathbf{n}})]$, meaning this relation is not one-to-one. An overview of this embedding is presented in Fig. 3, and details on the parametrization of these spaces can be found in section "Parametrization of the Special Euclidean Group".

2.1.1 Relating Functions on the Group to Functions on the Quotient

To distinguish functions on $SE(3)$ from functions on $\mathbb{R}^3 \rtimes S^2$ and $\mathbb{R}^3 \times S^2$ (which are homeomorphic), the former are denoted $\tilde{U}$ instead of U:

$$\tilde{U} : SE(3) \to \mathbb{R}^+ : (\mathbf{x}, Q) \mapsto \tilde{U}(\mathbf{x}, Q).$$

Following Eqs. (4) and (5), we identify $\tilde{U}$ with a function $U : \mathbb{R}^3 \rtimes S^2 \to \mathbb{R}^+$ according to

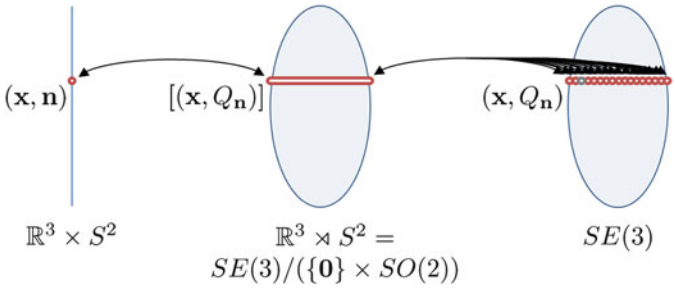

Fig. 3 The quotient $\mathbb{R}^3 \rtimes S^2$ consists of equivalence classes of $SE(3)$ and is homeomorphic to the original space of diffusion images $\mathbb{R}^3 \times S^2$

$$\begin{aligned} U(\mathbf{x}, \mathbf{n}) &= \tilde{U}(\mathbf{x}, Q_{\mathbf{n}}), \\ \tilde{U}(\mathbf{x}, Q) &= U(\mathbf{x}, Q.\mathbf{e}_z), \end{aligned} \tag{6}$$

for all $\mathbf{x} \in \mathbb{R}^3$ and all $Q \in SO(3)$. Recalling Eq. (3), we note that identification is unique if and only if we restrict ourselves to functions on the group with the following invariance property:

$$\tilde{U}(\mathbf{x}, Q) = \tilde{U}(\mathbf{x}, Q.Q_{\mathbf{e}_z,\alpha}), \tag{7}$$

for all $\alpha \in [0, 2\pi)$. If this requirement is not met there is no logical way to choose a function value out of $\{\tilde{U}(g) \mid g \in [(\mathbf{x}, Q_{\mathbf{n}})]\}$ to assign to $U(\mathbf{x}, \mathbf{n})$. The fact that operators on functions on $SE(3)$ have to preserve this property for the resulting functions to be properly defined on the quotient limits the set of possible functions, as will be discussed in the next section.

2.2 *Operator Legality*

If we want to define well-behaving operators on functions on $\mathbb{R}^3 \rtimes S^2$, it is good practice to impose Euclidean-invariance, i.e. invariance of the operator with respect to translations and rotations. Since all operators will first be defined on $SE(3)$, operators are additionally required to be α-invariant, a necessary property that follows from Eq. (3) and that ensures a unique relation between operators on $SE(3)$ and $\mathbb{R}^3 \rtimes S^2$. To define these invariances we define the left- and right group actions

$$\begin{aligned} L_g &: h \mapsto L_g(h) = gh, \\ R_g &: h \mapsto R_g(h) = hg, \end{aligned}$$

and the corresponding operators on a function $\tilde{U}$ by

$$(\mathscr{L}_g \circ \tilde{U})(h) = (\tilde{U} \circ L_g^{-1})(h) = \tilde{U}(g^{-1}h),$$
$$(\mathscr{R}_g \circ \tilde{U})(h) = (\tilde{U} \circ R_g)(h) \;\; = \tilde{U}(hg),$$

for all $g, h \in SE(3)$ and with $\circ$ function composition. $\mathscr{L}$ and $\mathscr{R}$ are respectively called the left- and right-regular representations, as they satisfy

$$\mathscr{L}_g \mathscr{L}_h = \mathscr{L}_{gh} \text{ and } \mathscr{R}_g \mathscr{R}_h = \mathscr{R}_{gh}$$

for all $g, h \in SE(3)$.

2.2.1 α-Invariance

In order to ensure that operators $\tilde{\Phi}$ acting on functions on the group respect the quotient structure depicted in Fig. 3, we must impose invariance under an additional rotation $Q_{\mathbf{e}_z,\alpha}$ from the right. Recall again Eq. (3). This α-invariance is the operator-equivalent of Eq. (7), and requires essentially that any operator $\tilde{\Phi}$ must satisfy

$$\mathscr{R}_g \circ \tilde{\Phi} = \tilde{\Phi} \tag{8}$$

for all $g = (\mathbf{0}, Q_{\mathbf{e}_z,\alpha}) \in (\{\mathbf{0}\} \times SO(2))$.

2.2.2 Left-Invariance

Euclidean-invariance now can be achieved by imposing invariance with respect to either left-regular representations (left-invariance), right-regular representations (right-invariance), or both. It turns out that only $\mathscr{L}_g$ is α-invariant, which along with arguments presented in the PhD thesis of Franken [27, Sect. 7.4.3] shows that for this case only left-invariance should be considered. Hence the invariance-imposed restriction is that every operator $\tilde{\Phi}$ acting on a function $\tilde{U}$ must commute with $\mathscr{L}_g$ for all $g \in SE(3)$:

$$\tilde{\Phi} \circ \mathscr{L}_g = \mathscr{L}_g \circ \tilde{\Phi}. \tag{9}$$

This requirement immediately guarantees Euclidean-invariance of the corresponding operator Φ defined on $\mathbb{R}^3 \rtimes S^2$ by means of Eq. (5).

2.2.3 Legal Operators

Operators on functions defined on $SE(3)$ are called legal if they correspond uniquely to well-defined operators on $\mathbb{R}^3 \rtimes S^2$, meaning they satisfy both Eqs. (8) and (9). Note that any concatenation and linear combination of legal operators is again legal.

2.3 The Moving Frame of Reference

We now define for each pair of a position and an orientation $(\mathbf{x}, \mathbf{n})$, a local frame of vectors aligned both spatially and angularly with $\mathbf{n}$. This enables us to define derivatives in a coordinate frame relative to $(\mathbf{x}, \mathbf{n})$, which ultimately allows us to define erosion at $\mathbf{x}$ towards fibers oriented along $\mathbf{n}$. As we do this for all $(\mathbf{x}, \mathbf{n})$ in the data set $(\mathbf{x}, \mathbf{n}) \mapsto U(\mathbf{x}, \mathbf{n})$, we can erode towards likely fibers present in the data.

As we have identified $\mathbb{R}^3 \times S^2$ with $SE(3)$, this frame can be expressed conveniently on the group $SE(3)$ first. From a geometrical point of view, this boils down to the definition of a moving frame of reference on the manifold $SE(3)$, which is simply a collection of vector fields that span the tangent spaces at each point on the manifold. The erosion operator that we will define in the next section will be expressed in terms of these vector fields.

Remark 1. Vector fields can always be considered as differential operators on locally defined smooth functions [3].

Because we plan to use the moving frame to define an erosion evolution, it is convenient to already incorporate left-invariance. That way any linear combination of these vector fields will be left-invariant as well, meaning we will only have to deal with α-invariance in order to assure legality. The left-invariant vector fields can be generated from any basis of the tangent space at the unity element (the Lie algebra). Here we will adhere to the following basis vectors at the unity element $e = (\mathbf{0}, I)$:

$$A_1 = \partial_x|_e, A_2 = \partial_y|_e, A_3 = \partial_z|_e, A_4 = \partial_{\tilde{\gamma}}|_e, A_5 = \partial_{\tilde{\beta}}|_e, A_6 = \partial_{\tilde{\alpha}}|_e,$$

where $\partial_{x^i}|_g \tilde{U} = \frac{\partial \tilde{U}}{\partial x^i}(g) \equiv \partial_i|_g \tilde{U}$, and where the variables of differentiation come from the second parameterization chart given in section "Parametrization of the Special Euclidean Group". Writing $\mathscr{A}_i|_g$ for the ith basis vector at $g \in SE(3)$, we obtain the left-invariant vector fields through the push-forward of the left group action [10] (Fig. 4),

$$\mathscr{A}_i|_g \tilde{U} = (L_g)_*(A_i)\tilde{U} \equiv A_i(\tilde{U} \circ L_g).$$

The dependence of the tangent vectors (and their duals) on the group element g will from hereon be omitted for readability where possible.

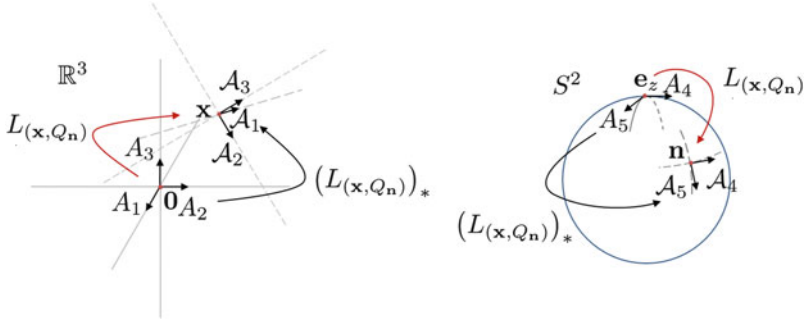

Fig. 4 A schematic representation of the five primary local frame vectors. Movement in the direction of $\mathscr{A}_6$ produces a simultaneous rotation of $\mathscr{A}_1$ and $\mathscr{A}_2$ around $\mathscr{A}_3$, and of $\mathscr{A}_4$ and $\mathscr{A}_5$ around $\mathbf{n} \equiv \mathscr{A}_3$. Since all functions we consider satisfy Eq. (7), $\mathscr{A}_6\tilde{U} = 0$. Because of this $\mathscr{A}_6$ is not illustrated, but it may be envisioned in the figure as the normal to the plane span$\{\mathscr{A}_4, \mathscr{A}_5\}$

Remark 2. Note that since we have defined $Q_\mathbf{n}.\mathbf{e}_z = \mathbf{n}$, the spatial generator $\mathscr{A}_3|_{(\mathbf{x},Q_\mathbf{n})}$ is always aligned with $\mathbf{n}$, i.e. $n^1\partial_x + n^2\partial_y + n^3\partial_z = \mathscr{A}_3|_{(\mathbf{x},\mathbf{n})}$ where $(n^1, n^2, n^3)^T = \mathbf{n}$ and $(x, y, z)^T = \mathbf{x}$.

Remark 3. In both charts, we have that the final angles α and $\tilde{\alpha}$ are in fact redundant, cf. Eq. (7) and the appendix.

The stated definition of the left-invariant vector fields may also be obtained by taking the derivative of the right-regular representation $\mathscr{R}$, cf. [18] which gives the alternative, more manageable expression

$$\mathscr{A}_i|_g\tilde{U} = (\mathrm{d}\mathscr{R}(A_i)\tilde{U})(g) = \lim_{t\downarrow 0}\frac{\tilde{U}(g\mathrm{e}^{tA_i}) - \tilde{U}(g)}{t}. \tag{10}$$

Here the exponential map takes a vector in the tangent space at e to an open subset Ω_e of the manifold around e, i.e. $\exp : T_e(SE(3)) \to \Omega_e$, see Fig. 5. As it can be shown that this maps $T_e(SE(3))$ bijectively onto $SE(3)$, we may take $\Omega_e = SE(3)$. Explicit expressions for the left-invariant vector fields, their duals, the exponential map, and its inverse, can all be found in previous work [21].

The corresponding frames on $\mathbb{R}^3 \times S^2$ are given by Duits et al. [20]

$$\begin{aligned}
\mathscr{A}_1U(\mathbf{x},\mathbf{n}) &= \lim_{h\downarrow 0}\tfrac{U(\mathbf{x}+hQ_\mathbf{n}\mathbf{e}_x,\mathbf{n})-U(\mathbf{x},\mathbf{n})}{h}\\
\mathscr{A}_2U(\mathbf{x},\mathbf{n}) &= \lim_{h\downarrow 0}\tfrac{U(\mathbf{x}+hQ_\mathbf{n}\mathbf{e}_y,\mathbf{n})-U(\mathbf{x},\mathbf{n})}{h}\\
\mathscr{A}_3U(\mathbf{x},\mathbf{n}) &= \lim_{h\downarrow 0}\tfrac{U(\mathbf{x}+hQ_\mathbf{n}\mathbf{e}_z,\mathbf{n})-U(\mathbf{x},\mathbf{n})}{h}\\
\mathscr{A}_4U(\mathbf{x},\mathbf{n}) &= \lim_{h\downarrow 0}\tfrac{U(\mathbf{x},Q_\mathbf{n}Q_{\mathbf{e}_x,h}\mathbf{e}_z)-U(\mathbf{x},\mathbf{n})}{h}\\
\mathscr{A}_5U(\mathbf{x},\mathbf{n}) &= \lim_{h\downarrow 0}\tfrac{U(\mathbf{x},Q_\mathbf{n}Q_{\mathbf{e}_y,h}\mathbf{e}_z)-U(\mathbf{x},\mathbf{n})}{h}
\end{aligned}$$

This definition will be used for the implementation, but we will for now continue with the vector fields $\{\mathscr{A}_i\}_{i=1}^6$ defined on $SE(3)$.

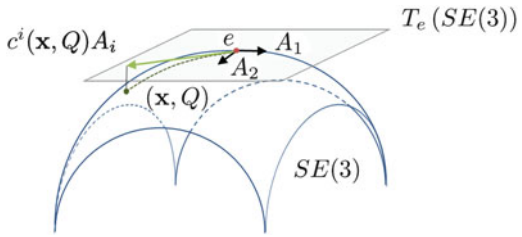

Fig. 5 A simplified diagram of the algebraic structure discussed in this chapter. The bent surface represents $SE(3)$, with the unity element e indicated by the *red dot*. The tangent surface $T_e(SE(3))$ is the set of the Lie algebra, with the basis $\{A_i\}_{i=1}^6$, of which for obvious reasons only the first two are shown. The *green arrow* is a random tangent vector $c^i(\mathbf{x}, Q)A_i$ at the unity element, where $c^i(\mathbf{x}, Q)A_i \xrightarrow{\exp} (\mathbf{x}, Q)$

Remark 4. Note that $\{\mathscr{A}_i\}_{i=1}^5$ are well-defined vector fields on $\mathbb{R}^3 \times S^2$ but *not* on $\mathbb{R}^3 \rtimes S^2$, since $\{\mathscr{A}_i\}_{i\in\{1,2,4,5\}}$ depend on the redundant angle α.

2.4 Legal Metrics

The left-invariant vector fields induce a set of metrics on $SE(3)$. By definition, any metric on $SE(3)$ can be written in the form

$$\mathbf{G}|_{(\mathbf{x},Q)} = \sum_{i,j=1}^{6} g_{ij}(\mathbf{x}, Q)\, \omega^i|_{(\mathbf{x},Q)} \otimes \omega^j|_{(\mathbf{x},Q)}. \tag{11}$$

Here $\omega^i|_{(\mathbf{x},Q)}$ denotes[1] the dual of the ith basis vector of the tangent space at $(\mathbf{x}, Q) \in SE(3)$, with the defining property

$$\omega^i\left(\sum_{j=1}^{6} c^j \mathscr{A}_j\right) = c^i.$$

The coefficients $\{g_{ij}\}_{i,j=1}^6$ represent the relative penalty associated with moving in the corresponding direction $\mathscr{A}_i$, and are subject to the constraint[2]

$$[g_{ij}] = \mathrm{diag}(D^{11}, D^{11}, D^{33}, D^{44}, D^{44}, D^{66})^{-1}, \quad D^{ii} \in \mathbb{R}^+, \tag{12}$$

[1] In previous work we wrote $d\mathscr{A}^i$ for the dual vectors, but to avoid possible confusion with the exterior derivative operator we use ω^i here.

[2] We take here D^{ii} to be constant. This is not strictly necessary, and taking $D^{ii}(\tilde{U})$ can in fact be useful [20].

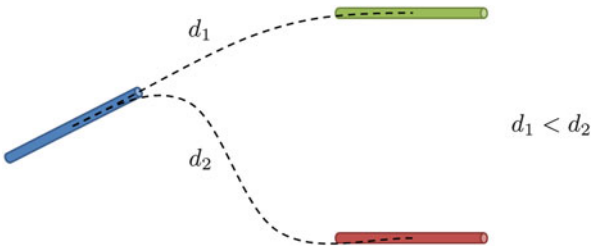

Fig. 6 An example of the use of a sub-Riemannian metric. By prohibiting motion perpendicular to the fiber fragment, we find a distance measure that allows us to distinguish between the aligned and the misaligned glyph of Fig. 2. The *dotted lines* are projections of two (estimated) solutions to Eq. (13) onto $\mathbb{R}^3 \times S^2$

so as to ensure legality [20]. Since any movement along $\mathscr{A}_6$ can be considered null (see Remark 3), we neglect D^{66}.

As an example, assume that $D^{33} = D^{44}$, meaning the distance increases equally with an equal movement in either $\mathscr{A}_3$, $\mathscr{A}_4$, or $\mathscr{A}_5$. Furthermore, we prohibit movement in the directions $\mathscr{A}_1$ and $\mathscr{A}_2$ by taking $D^{11} \downarrow 0$. Note that this implies infinite cost for movement in the plane $\text{span}\{\mathscr{A}_1, \mathscr{A}_2\}$, perpendicular to the spatial propagation direction $\mathscr{A}_3$. This last decision means we are now considering a distance on a sub-Riemannian manifold [5] $B := (SE(3), \ker\{\omega^1\} \cap \ker\{\omega^2\} \cap \ker\{\omega^3\}, \sum_{i=3}^{5} \left(D^{ii}\right)^{-1} \omega^i \otimes \omega^i)$. The distance between two points $g_1, g_2 \in SE(3)$, and the corresponding distance in $\mathbb{R}^3 \times S^2$, is then given by the shortest smooth connecting curve $\bar{\gamma} : [0, L] \to SE(3)$ defined on B (Fig. 6):

$$\mathrm{d}(g_1, g_2) = \inf_{\substack{\bar{\gamma} \in C^\infty([0,L],B),\\ \bar{\gamma}(0) = g_1,\ \bar{\gamma}(L) = g_2,\\ \dot{\bar{\gamma}}^1(s) = \dot{\bar{\gamma}}^2(s) = \dot{\bar{\gamma}}^6(s) = 0}} \int_0^L \sqrt{\frac{1}{D^{33}} \dot{\bar{\gamma}}^3(s)^2 + \frac{1}{D^{44}} (\dot{\bar{\gamma}}^4(s)^2 + \dot{\bar{\gamma}}^5(s)^2)}\, ds. \tag{13}$$

While this illustrates the possibilities of the presented theory, it is an entirely different optimal control problem [15] than the one needed for sharpening. Below we will use another configuration of parameters, giving rise to a different sub-Riemannian manifold and metric tensor that when used to generate an evolution equation, results in the $\mathbb{R}^3 \times S^2$-analogue of typical spatial erosion evolutions.

2.5 Overview

In summary, we have argued that DW-MRI data sets should be considered functions on the coupled space $\mathbb{R}^3 \rtimes S^2$, whose natural group structure follows from embedding the space in the group of three dimensional rigid motions $SE(3)$. By

posing that operators on DW-MRI data should be invariant under rotations and translation, and need to satisfy α-invariance, Eq. (8), we defined a requirement for operators to be 'legal'. We then proceeded to describe a left-invariant moving frame of reference on $SE(3)$, which allows us to look at the data as if attached to a local fiber fragment. This moving frame is then used to describe the range of possible legal metrics, which we can use in the next section to define the erosion operator.

3 Erosion

At an elementary level, morphological operations on $\mathbb{R}^n$ can be considered solutions to a specific class of evolution equations [50]. Writing $f : \mathbb{R}^n \to \mathbb{R}^+$ for the gray value image and $m : \mathbb{R}^n \to \mathbb{R}^+$ for the structuring element, the morphological convolution $h : \mathbb{R}^n \to \mathbb{R}^+$ that solves the erosion equation (which depends on the structuring element m), is given by

$$h(\mathbf{x}) = (f \ominus m)(\mathbf{x}) := \inf_{\mathbf{y}\in\mathbb{R}} [f(\mathbf{y}) + m(-\mathbf{y} + \mathbf{x})]. \tag{14}$$

In case the structuring element satisfies the semi-group property [6, 53], the PDE satisfied by h dictates a morphological scale-space. If for example m is a quadratic structuring element, i.e. of the form $m_t(\mathbf{x}) = \frac{2\eta-1}{2\eta}\left(\frac{\|\mathbf{x}\|^{2\eta}}{t}\right)^{\frac{1}{2\eta-1}}$, where $\eta \in \left(\frac{1}{2}, 1\right]$ and $t \in \mathbb{R}^+$, then the size t of the structuring element parameterizes a morphological scale space [6, 31, 53] dictated by the evolution equation

$$\begin{cases} \partial_t h(\mathbf{x}; t) = -\frac{1}{2\eta}\|\nabla h(\mathbf{x}; t)\|^{2\eta}, \\ h(\mathbf{x}; 0) = f(\mathbf{x}). \end{cases}$$

In generalizing these results to $SE(3)$ we start from the premise that erosion is described by one of the legal scale spaces that can be defined on that group. Similar scale-spaces can be constructed [17] by employing the previously defined general metric. This yields for $g \in SE(3)$ and $t \geq 0$

$$\begin{cases} \partial_t \tilde{W}(g; t) = \pm\frac{1}{2\eta}\left[\mathbf{G}|_g^{-1}\left(d\tilde{W}(g; t), d\tilde{W}(g; t)\right)\right]^{\eta}, \\ \tilde{W}(g; 0) = \tilde{U}(g), \end{cases} \tag{15}$$

where $\tilde{W}(.; t)$ is the function on the Lie group $SE(3)$, initially given by the original data $\tilde{U} : SE(3) \to \mathbb{R}^+$, $d\tilde{W}(g; t) = \sum_{i=1}^{6} \mathscr{A}_i \tilde{W}(g; t)\omega^i$ is the gradient of $\tilde{W}$, and

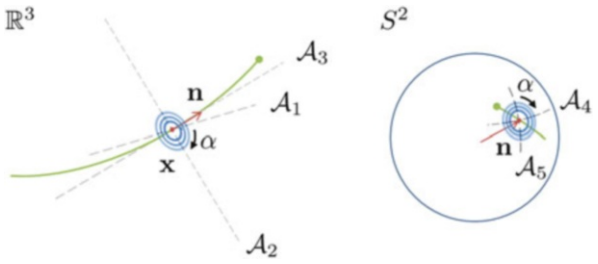

Fig. 7 A schematic showing the rationale behind the choice $D^{33} = 0$ when considering erosion. Since $\mathscr{A}_3$ is oriented along the fiber fragment, one prefers to erode *only* perpendicular to this direction, as indicated by the *blue circles*. Note that the depicted fiber represents *any* potential fiber passing through **x** with orientation **n**

G is the left-invariant metric tensor given in Eq. (11) with the coefficients $D^{ii} \in \mathbb{R}^+$ as in Eq. (12). Different choices[3] for the coefficients result in different scale spaces.

3.1 Erosion Towards Fibers

Proper choices for D^{11}, D^{33} and D^{44} are easily 'guessed' from their relation to the moving frame of reference. As illustrated in Fig. 7, erosion should transport data surrounding a fiber (i.e. perpendicular to $\mathscr{A}_3$) towards it, both spatially and angularly. This means that we need to take $D^{33} = 0$ while D^{11} and D^{44} are still free, and that we should look at the minus case of Eq. (15). The resulting differential equation is the Hamilton-Jacobi-Bellman equation

$$\begin{cases} \partial_t \tilde{W}(g;t) = -\frac{1}{2\eta}\left[D^{11}\left((\mathscr{A}_1\tilde{W}(g;t))^2 + (\mathscr{A}_2\tilde{W}(g;t))^2\right) + \right. \\ \qquad\qquad \left. D^{44}\left((\mathscr{A}_4\tilde{W}(g;t))^2 + (\mathscr{A}_5\tilde{W}(g;t))^2\right)\right]^{\eta}, \\ \tilde{W}(g;0) = \tilde{U}(g), \end{cases} \tag{16}$$

with again $\eta \in \left(\frac{1}{2}, 1\right]$. The proof showing that this evolution equation can be solved by a morphological convolution,[4] and can thus be qualified as an erosion, is fairly technical and will not be given here, but can be found online [20].

[3]The values allowed for the coefficients are subject to the Hörmander requirement [30] which guarantees smooth non-singular scale spaces. Proofs that the evolutions presented here satisfy this condition are available [20].

[4]The morphological convolution is in fact the viscosity solution to the morphological scale space, similar to the same problem on $\mathbb{R}^n$ [11,24] and on the Heisenberg group $H(n)$ [35].

In complete analogy to the problem in $\mathbb{R}^n$, there exists a structuring element, or kernel, $\tilde{k}_t^{D^{11},D^{44}} : SE(3) \to \mathbb{R}^+$, such that

$$\tilde{W}(g;t) = (\tilde{U} \ominus_{SE(3)} \tilde{k}_t^{D^{11},D^{44}})(g),$$

with $\ominus_{SE(3)}$ denoting the $SE(3)$-counterpart to the erosion operator defined in Eq. (14), given by

$$(\tilde{U} \ominus_{SE(3)} \tilde{k}_t^{D^{11},D^{44}})(g) := \inf_{h \in SE(3)} \left[\tilde{U}(h) + \tilde{k}_t^{D^{11},D^{44}}(h^{-1}g) \right], \tag{17}$$

which fits in the framework of group morphology [44]. As shown in other work [6, 19], $\tilde{k}_t^{D^{11},D^{44}}$ is the morphological Green's function, which may be approximated by

$$\tilde{k}_t^{D^{11},D^{44}}(g) \approx \frac{2\eta - 1}{2\eta} \frac{\left(C^2 \sqrt{\frac{(c^3)^2}{D^{11}D^{44}} + \frac{(c^6)^2}{D^{44}D^{44}} + \left(\frac{(c^1)^2+(c^2)^2}{D^{11}} + \frac{(c^4)^2+(c^5)^2}{D^{44}} \right)^2} \right)^{\frac{\eta}{2\eta-1}}}{t^{\frac{1}{2\eta-1}}}, \tag{18}$$

where we use short-hand notation $\{c^i\}_{i=1}^6 = \{c^i(g)\}_{i=1}^6$ coming from the logarithm on $SE(3)$, cf. Fig. 5, of which explicit expression can be found in section "The Logarithmic Map". The constant $C \in (0, 2]$ comes along with the Heisenberg approximation technique [22, 37] used in deriving the expression, and can be considered a simple reparameterization of t. A direct consequence of the fact that the erosion operator on $SE(3)$ is a solution to Eq. (16), is that the morphological convolution given satisfies the semi-group property, i.e.

$$\left((\tilde{U} \ominus_{SE(3)} \tilde{k}_s^{D^{11},D^{44}}) \ominus_{SE(3)} \tilde{k}_t^{D^{11},D^{44}} \right)(g) = (\tilde{U} \ominus_{SE(3)} \tilde{k}_{s+t}^{D^{11},D^{44}})(g)$$

A fairly basic example of erosion is shown in Fig. 8b, where a column of aligned glyphs is surrounded by glyphs with random orientations. The operation significantly decreases the function value for misaligned fiber fragments.

3.2 Minimum Reduction

One property the DW-MRI erosions inherited from the regular $\mathbb{R}^n$ morphological operations, is that bounds on the function given by the extrema are retained. Erosion decreases values that lie near a minimum, but as follows from the fact that the solutions are given by a morphological convolution, they will always remain between the global minimum and maximum. While this guarantees well-posedness and stability with respect to the $\mathbb{L}^\infty$-norm (in contrast to for instance deconvolution

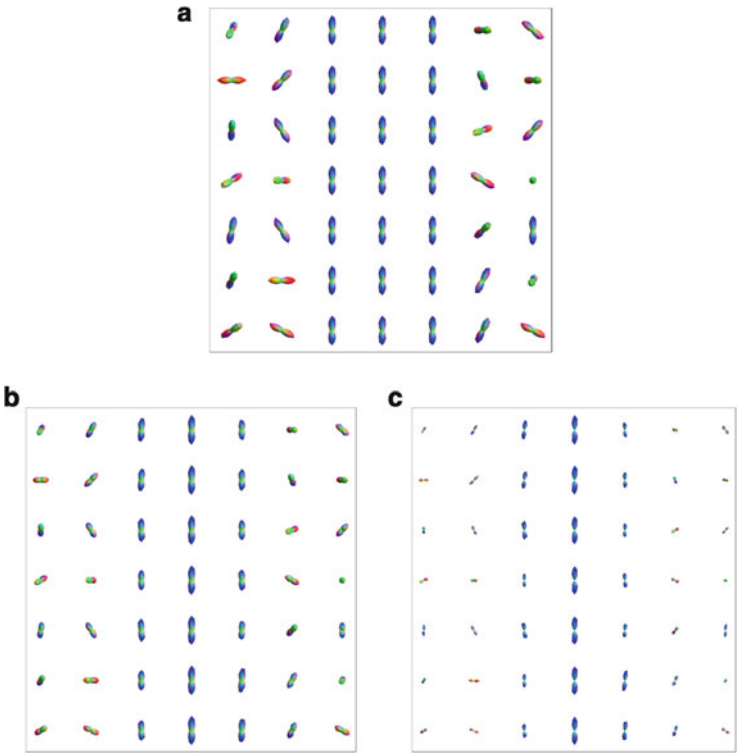

Fig. 8 A basic example of erosion with manually selected parameters ($\Delta t = 0.02$, $D^{11} = 0.5$ and $D^{44} = 0.02$). (**a**) A slice of an artificial data set containing a number of aligned glyphs, surrounded by randomly oriented glyphs. (**b**) The data from (**a**) after erosion, with $t = 3$ and $\eta = 0.75$. (**c**) The data from (**a**) after min-normalization and erosion, with $t = 4$ and $\eta = 0.65$

operators), the drawback of this is that we can not decrease minima even if they seem to be misrepresentative of the local structure. We have previously attempted to resolve this by min-normalizing the data before eroding [14,20]. min-normalization $\nu_{\min}$ of a data set $\tilde{U} : SE(3) \to \mathbb{R}^+$ is defined as

$$\nu_{\min}(\tilde{U})(\mathbf{x}, \mathbf{n}) = \tilde{U}(\mathbf{x}, \mathbf{n}) - \min\{\tilde{U}(\mathbf{x}, \mathbf{n}') | \mathbf{n}' \in S^2\}. \tag{19}$$

The effect of this operation on subsequent erosions is depicted in Fig. 8c. The normalization essentially increases the contrast per glyph, effectively sharpening the data angularly.

A more prevalent approach to angular sharpening in the literature is the $(I - a\Delta_{LB})$ operator, which subtracts the result of the Laplace-Beltrami operator Δ_{LB} scaled by $a \in \mathbb{R}^+$ from the original data:

$$v_{LB}(\tilde{U})(\mathbf{x},\mathbf{n}) = \tilde{U}(\mathbf{x},\mathbf{n}) - a(\Delta_{LB}\tilde{U})(\mathbf{x},\mathbf{n}). \tag{20}$$

In our framework, the Laplace-Beltrami operator is given by

$$\Delta_{LB} = (\mathscr{A}_4)^2 + (\mathscr{A}_5)^2 + (\mathscr{A}_6)^2,$$

where the last term can of course be neglected as we have $(\mathscr{A}_6)^2\tilde{U} = 0$, recall Remark 3.

Remark 5. The Laplace-Beltrami operator is a legal operator, as the α dependence of $\mathscr{A}_4$ and $\mathscr{A}_5$ cancels out in Eq. (3.2).

3.3 Approximating Solutions

We have considered two different approaches to implement erosions for DW-MRI data. The first one is based on the group-convolution with the approximation of the Green's function, Eq. (18), while the second one directly discretizes the Hamilton-Jacobi-Bellman equation that governs erosion, Eq. (16). Both the implementations are included in a Mathematica package available for academic purposes at www.bmia.bmt.tue.nl/people/RDuits/DWIpackage/HARDIAlgorithms.zip. Details of the implementation are briefly outlined below.

3.3.1 Convolutions

In order to approximate the solutions to the erosion equation, we can choose to compute the morphological convolution of Eq. (17) using a discretized version of the erosion kernel. Since we know that due to α-invariance the kernel will be independent of any variation in the redundant angle $\tilde{\alpha}$ (or α in the first chart, section "Parametrization of the Special Euclidean Group"), we can reduce the convolution on $SE(3)$ to

$$(k_t^{D^{11},D^{44}} \ominus_{\mathbb{R}^3\times S^2} U)(g) := \inf_{h\in\mathbb{R}^3\times S^2}\left[U(h) + k_t^{D^{11},D^{44}}(h^{-1}g)\right].$$

where we define the kernel $k_t^{D^{11},D^{44}} : \mathbb{R}^3 \times S^2 \to \mathbb{R}^+$ in terms of $\tilde{k}_t^{D^{11},D^{44}}$ by

$$k_t^{D^{11},D^{44}}(\mathbf{x},\mathbf{n}) := \tilde{k}_t^{D^{11},D^{44}}(\mathbf{x}, Q_{\mathbf{n}}),$$

for any $Q_{\mathbf{n}}$ such that $Q_{\mathbf{n}}.\mathbf{e}_z = \mathbf{n}$.

3.3.2 Discretizing the Problem

Alternatively we can discretize the scale-space equation directly. The initial condition $\tilde{W}(g;0) = \tilde{U}(g)$ of course remains, and the left-hand side of the differential equation becomes

$$\partial_t \tilde{W}(g;t) = \lim_{dt\to 0} \frac{\tilde{W}(g;t+dt) - \tilde{W}(g;t)}{dt} \approx \frac{\tilde{W}(g;t+\Delta t) - \tilde{W}(g;t)}{\Delta t}$$

with Δt small, resulting in the incremental algorithm

$$\tilde{W}(g;t+\Delta t) = \tilde{W}(g;t) \pm \Delta t \frac{1}{2\eta} \left[\mathbf{G}|_g^{-1} \left(d\tilde{W}(g;t), d\tilde{W}(g;t) \right) \right]^{\eta}.$$

In the specific case we are considering here (see Sect. 3.1), we thus get

$$\begin{cases} \tilde{W}(g;t+\Delta t) = \tilde{W}(g;t) - \Delta t \frac{1}{2\eta} \left[D^{11} \left((\mathscr{A}_1 \tilde{W}(g;t))^2 + (\mathscr{A}_2 \tilde{W}(g;t))^2 \right) + \right. \\ \qquad\qquad \left. D^{44} \left((\mathscr{A}_4 \tilde{W}(g;t))^2 + (\mathscr{A}_5 \tilde{W}(g;t))^2 \right) \right]^{\eta}, \\ \tilde{W}(g;0) = \tilde{U}(g), \end{cases}$$

for $g \in SE(3)$, and where we still need to discretize the derivative $\mathscr{A}_i$. At this point we return once more to the space $\mathbb{R}^3 \times S^2$ by means of the identification in Eq. (6):

$$\begin{cases} W(\mathbf{x},\mathbf{n};t+\Delta t) = W(\mathbf{x},\mathbf{n};t) - \Delta t \frac{1}{2\eta} \left[D^{11} \left((\mathscr{A}_1 W(\mathbf{x},\mathbf{n};t))^2 + (\mathscr{A}_2 W(\mathbf{x},\mathbf{n};t))^2 \right) + \right. \\ \qquad\qquad \left. D^{44} \left((\mathscr{A}_4 W(\mathbf{x},\mathbf{n};t))^2 + (\mathscr{A}_5 W(\mathbf{x},\mathbf{n};t))^2 \right) \right]^{\eta}, \\ W(\mathbf{x},\mathbf{n};0) = U(\mathbf{x},\mathbf{n}), \end{cases}$$

We can follow the exact same procedure as before to get the stencils given in section "Finite Difference Schemes".

Remark 6. The spatial derivatives are in fact calculated using an upwind-biased finite differences scheme, see the appendix.

3.3.3 Two Implementations

We distinguished between two implementations for morphological scale spaces:

1. Erosion via convolutions with the approximations of the morphological Green's functions given by Eq. (18).
2. Erosion via left-invariant finite-difference (upwind) schemes, of which the details are provided in section "Finite Difference Schemes".

As explained in detail in Sect. 2.1, the non-commutative nature of $SE(3)$ leads to a natural coupling in the space $\mathbb{R}^3 \rtimes S^2$ of positions and orientations. As a result,

neither implementation is separable in a spatial and angular part, excluding the trivially separable cases where $D^{44}D^{11} = 0$.

Generally speaking, the advantages of the kernel implementations are:

- They allow fast parallel algorithms via lookup tables and precomputed Green's functions, similar to implementations [43] of linear $\mathbb{R}^3 \rtimes S^2$-convolutions [18].
- They are unconditionally stable and directly related to viscosity solutions, cf. [20].
- They involve less interpolation.

The advantages of the finite difference schemes are:

- They are much more flexible towards data adaptive extensions, cf. [14].
- They use efficient (short) stencils of interpolated finite differences, cf. [14].
- Do not involve analytic asymptotical approximations.

The implementations are complementary; the finite differences can be used for accurate precomputation of the Green's functions used in the convolution schemes. Both implementations are included in the *Mathematica* package available (for academic purposes only) at www.bmia.bmt.tue.nl/people/RDuits/DWIpackage/HARDIAlgorithms.zip.

Remark 7. All of the erosions shown in this article have been obtained using the finite differences approach. Note that apart from the scaling factor C of the time, the two methods produce approximately the same results.

4 Preprocessing with Erosion

Qualitative improvement by erosion has been shown before [20], and is reiterated in Fig. 9c. More interesting is the potential benefit of erosion for contextual operators. Figure 9 also shows the use of erosion as a processing step preceding hypo-elliptic diffusion [20].

As stated in the introduction, the most important contextual operators are tractography operators. Probabilistic tractography algorithms cope with data uncertainty by defining a distribution of fiber directions at each position [32, 33], and generate a large amount of pathways by sampling the directions around peaks of this distribution. Sharp and accurate glyphs that are aligned with their context will result in more reliable tractography. Alignment of glyphs is improved here by contour enhancement processes [18]. Since these processes generally propagate oriented particles in too many directions, an extra sharpening step is desired [20].

A challenging fiber bundle to extract is the optic radiation. This structure is part of the visual system, and connects the Lateral Geniculate Nucleus (LGN) to the primary visual cortex $V1$. The optic radiation has a curved anterior extent called Meyer's loop, which makes the fiber bundle difficult to reconstruct reliably. Other fiber bundles in its vicinity further complicate delineation. Direct application of

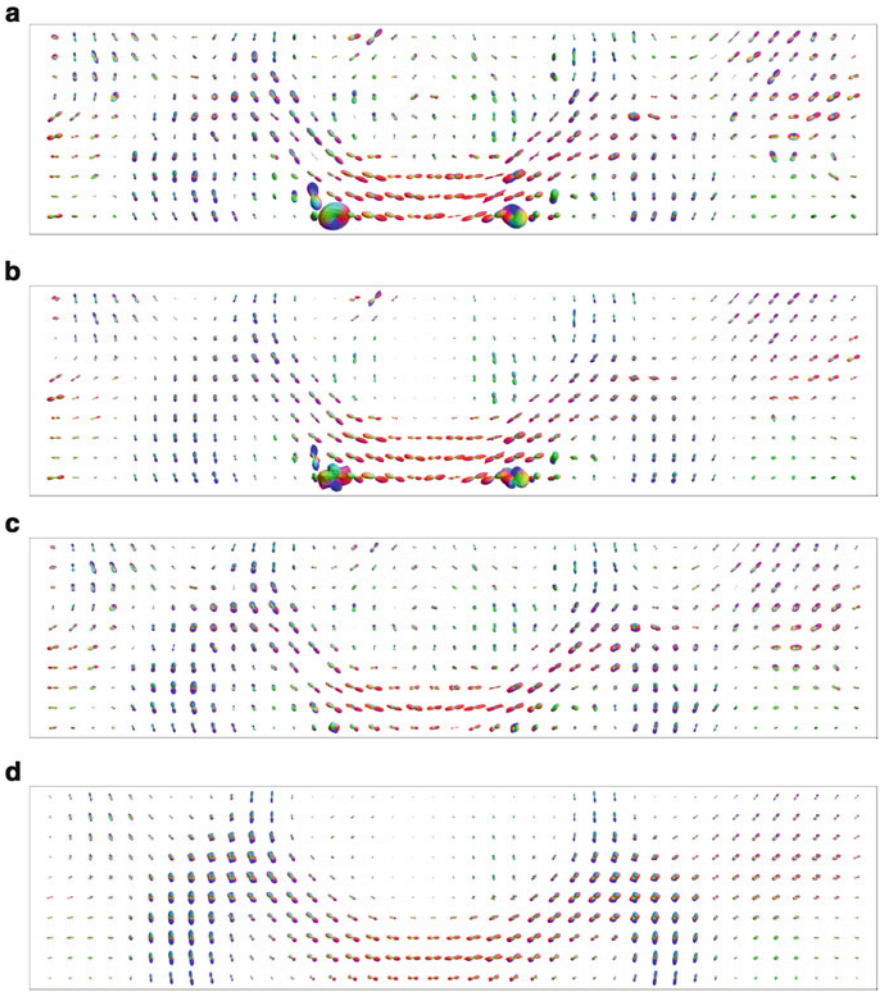

Fig. 9 A DW-MRI data set showing the corpus callosum and the corona radiata, before and after enhancement. Note especially the significant improvement of the enhancement when preceded by erosion. The enhancement was done using hypo-elliptic diffusion [20] with $t = 3$, $\Delta t = 0.01$, $D^{33} = 1$, $D^{44} = 0.002$ and $K = 0.05$. Erosion used $t = 3$, $\Delta t = 0.1$, $\eta = 0.75$, $D^{11} = 1$ and $D^{44} = 0.002$. All visualized data sets were min-normalized using Eq. (19). (**a**) A slice of the min-normalized original data. (**b**) The data from (**a**) after diffusion. (**c**) The data from (**a**) after erosion. (**d**) The data from (**a**) after erosion and diffusion

the reconstruction of this bundle lies in the context of neurosurgical planning for temporal lobe epilepsy. Meyer's loop is often located close to the area that causes epilepsy in these patients, and is disrupted during surgery. This can lead to visual loss of up to a quarter of the visual field.

To show the value of erosion as a preprocessing step for contextual enhancement and tractography, we evaluated the reliability of pathways resulting from a probabilistic tractography algorithm [45] both before and after erosion. The tractography algorithm generates 10^4 tracts based on DTI data[5] using a bootstrapping procedure [23]. We score each pathway $\gamma : [0, L_\gamma] \to \mathbb{R}^3$ according to how well they fit the underlying data, obtained by evaluating U along the tangent vectors $\dot{\gamma} = \frac{d}{ds}\gamma$ of γ [49]:

$$\mathscr{E}_U(\gamma) = \frac{1}{L_\gamma} \int_0^{L_\gamma} \log \left[\frac{U\left(\gamma(s), \dot{\gamma}(s)\right)}{\max U} \right] ds, \tag{21}$$

where L_γ is the length of the pathway γ, and s denotes arc length such that $\dot{\gamma}(s) \in S^2$, i.e. $\|\dot{\gamma}(s)\| = 1$. The data sets are divided by their global maximum for the sake of comparison. The initial cost function U was obtained directly from the diffusion tensors according to Eqs. (1) and (2), where $p(\mathbf{x}) = 1_\Omega(\mathbf{x}) \frac{\sqrt{\det(D(\mathbf{x}))}}{\int_\Omega \sqrt{\det(D(\mathbf{x}))}\, d\mathbf{x}}$ is proportional to the volume of the glyphs. The indicator function 1_Ω is a white matter mask obtained by a fractional anisotropy threshold. The entire scoring pipeline is depicted in Fig. 10.

Figure 11 visualizes the 30, 3 and 0.3 % highest scoring fibers according to Eq. (21) based on the unprocessed data U, the data U pre-processed using only linear hypo-elliptic diffusion, and the data U after both erosion and diffusion. Before any processing, the data is min-normalized.

The method is considered adequate when two conditions are satisfied: on the one hand, the whole optic radiation should be visible (few false negatives), and on the other hand all auxiliary fibers that are not clearly part of the optic radiation should be removed (few false positives). Only when a critical percentage of highest scoring fibers exists that satisfies both conditions, the method is able to give a reliable reconstruction of the optic radiation. We see that only in the case that erosions are included as a preprocessing step, such a critical percentage can be found. In Fig. 11c, we satisfy the two conditions at 28.3 %. There a large portion of the additional fibers falsely identified as part of the optic radiation (false positives) in Fig. 11a, b are removed by the erosion step, which decreases the likelihood of the tracking algorithm finding fibers that deviate strongly from the main fiber orientation.

If we replace the min-normalization with the more common $(I - a\Delta_{LB})$ operator, we can again find a critical percentage at which the method can be considered adequate, though this percentage lies a lot lower than before, at 0.4 %. See also Fig. 12.

[5] Kindly provided by the Kempenhaeghe Epilepsy Center in Heeze, the Netherlands.

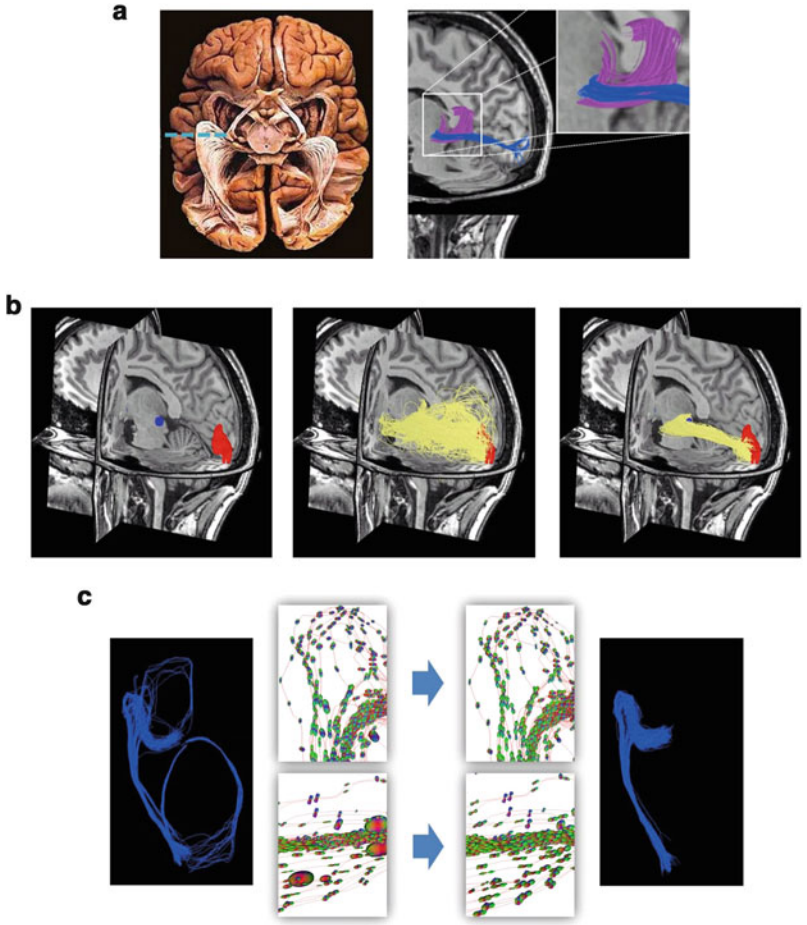

Fig. 10 The scoring pipeline. (**a**) In treating temporal lobe epilepsy, surgeons need to avoid the optic radiation to preserve the patient's vision. Tracking the optic radiation is challenging due to nearby and crossing fibers. (**b**) The optic radiation connects the LGN (blue) and V1 (red). The location of V1 is derived from functional MRI. Probabilistic tractography algorithms generate a large number of tracts between the visual cortex $V1$ and the LGN. These tracts are scored to filter out the optic radiation. (**c**) Enhancement: even with state of the art scoring, the tractography produces a lot of anatomically implausible tracts. Preprocessing the DW-MRI data with erosion and contextual enhancement greatly improves the segmentation of the optic radiation

5 Conclusion

In this paper we have demonstrated the benefits of erosion (well-posed sharpening) as a pre-processing step of contextual processing of Diffusion Weighted MRI. To this end, a Euclidean-invariant erosion evolution was defined on the space $\mathbb{R}^3 \rtimes S^2$

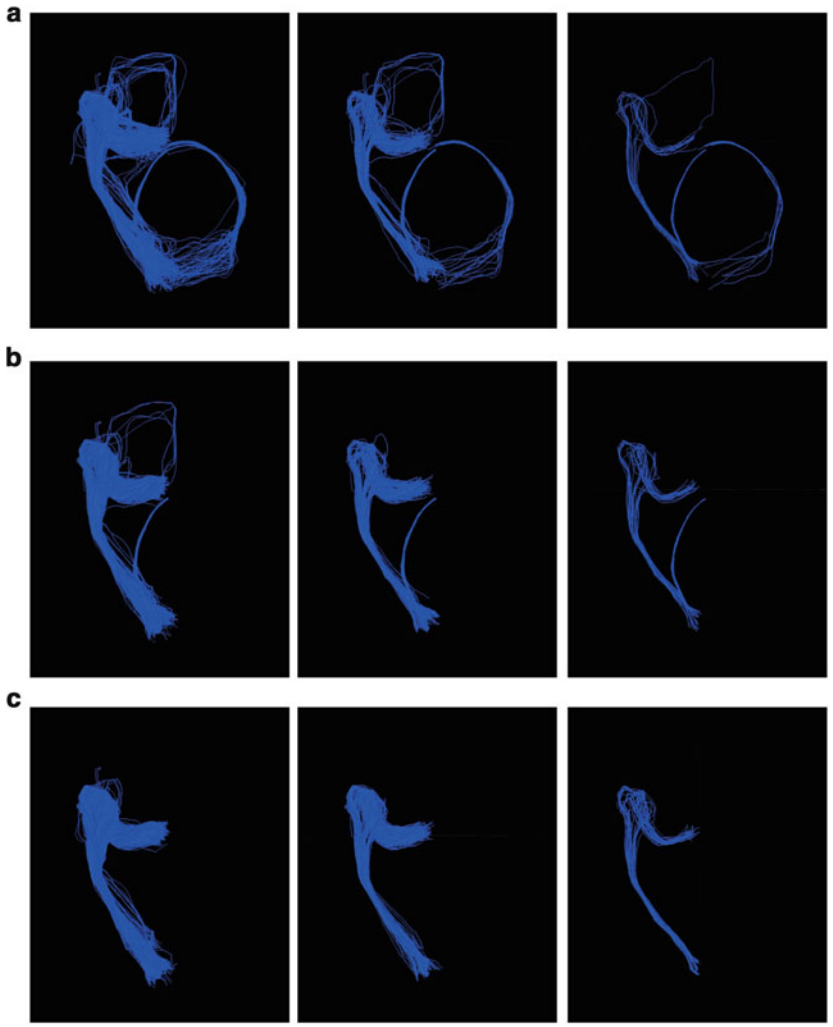

Fig. 11 Tracts obtained from a DTI data set, scored according to differently processed data sets. The hypo-elliptic diffusion has the following parameter settings: $t = 3$, $\Delta t = 0.01$, $D^{33} = 1$ and $D^{44} = 0.01$. Erosion has: $t = 3$, $\Delta t = 0.1$, $\eta = 0.75$, $D^{11} = 1$ and $D^{44} = 0.02$. (**a**) Tracts based on the original data. (**b**) Tracts based on the data from (**a**), following min-normalization and enhancement (hypo-elliptic diffusion). (**c**) Tracts based on the data from (**a**), after min-normalization, erosion, and enhancement

embedded as a quotient in $SE(3)$. The final erosion operator is the mapping that takes the initial condition of this evolution, generally the diffusion weighted image, to the (viscosity) solution with fixed time $t > 0$ of the evolution equation. These erosions satisfy the semi-group property.

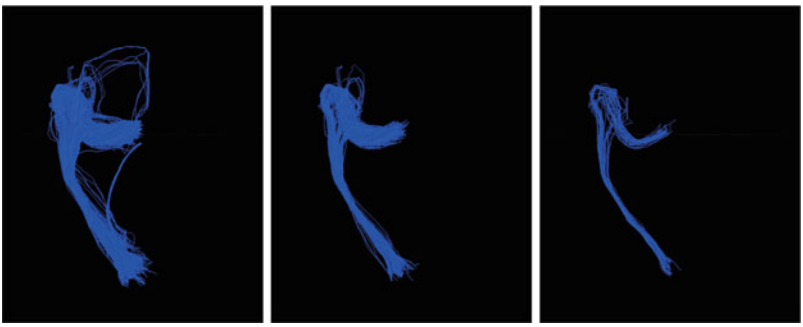

Fig. 12 Tracts obtained in the same way as in Fig. 11c, though the min-normalization is replaced by the minimum reduction technique of Eq. (20) with $a = 0.3$

We have presented two complementary numerical algorithms to compute the erosion operator, an analytical kernel implementation and a finite differences scheme, each with its own advantages.

We have shown the benefits of including erosions in contextual enhancement (via hypo-elliptic diffusion [20]) of DW-MRI. The erosion operator has been shown to visually sharpen the corpus callosum (the major fiber bundle connecting the two hemispheres) and corona radiata which crosses this major fiber bundle radially. See Fig. 9. Finally, we have shown that inclusion of erosions in pre-processing improves subsequent tracking of the optic radiation fibers in the brain, which is relevant for the planning of neurosurgery for epilepsy treatment [49], as shown in Fig. 11.

Parametrization of the Special Euclidean Group

Parametrization of the spatial part of $SE(3)$ is usually done by Cartesian coordinates and for the rotation part $SO(3)$ of $SE(3) = \mathbb{R}^3 \rtimes SO(3)$ we use two charts. Firstly, we use the standard Euler angle parametrization of the sphere given by

$$R = R_{\mathbf{e}_z,\gamma} R_{\mathbf{e}_y,\beta} R_{\mathbf{e}_z,\alpha},$$

with $\alpha \in [0, 2\pi)$, $\beta \in [0, \pi]$, $\gamma \in [0, 2\pi)$ and with $R_{\mathbf{v},\phi}$ a counter-clockwise rotation ϕ around the vector $\mathbf{v}$. The rotation axes are depicted in Fig. 13 obtained by applying the rotation to the unit vector oriented along the z-axis. A point $\mathbf{p} \in S^2$ can be identified with all rotations of $\mathbf{e}_z$ such that

$$\mathbf{p} = R_{\mathbf{p}} \mathbf{e}_z \equiv \mathbf{n}(\beta, \gamma), \tag{22}$$

with $R_{\mathbf{p}}$ any R that rotates $\mathbf{e}_z$ to $\mathbf{p}$ and where $\mathbf{n}$ is the parametrization. The parametrization is however ambiguous since

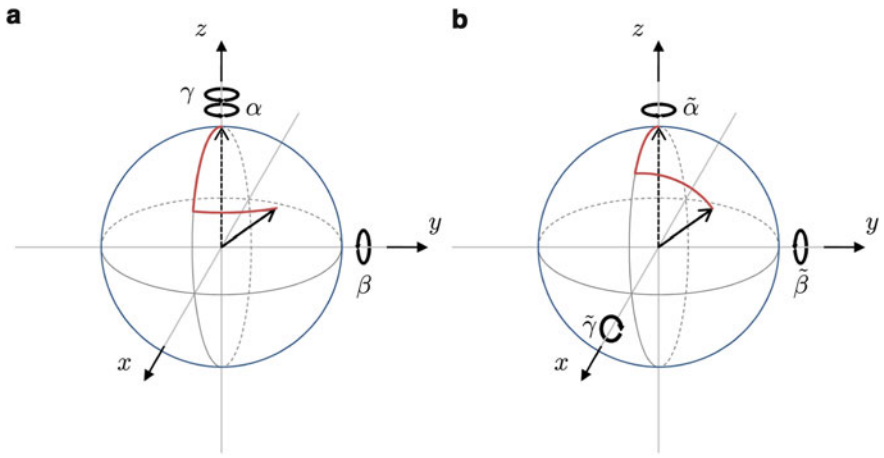

Fig. 13 The two different Euler parameterizations of $SO(3)$ and $S^2 \equiv SO(3)/SO(2)$. (**a**) *ZYZ* parametrization. (**b**) *ZYX* parametrization

$$R_{\mathbf{e}_z,\gamma} R_{\mathbf{e}_y,0} R_{\mathbf{e}_z,\alpha} = R_{\mathbf{e}_z,\gamma+\delta} R_{\mathbf{e}_y,0} R_{\mathbf{e}_z,\alpha-\delta},$$
$$R_{\mathbf{e}_z,\gamma} R_{\mathbf{e}_y,\pi} R_{\mathbf{e}_z,\alpha} = R_{\mathbf{e}_z,\gamma+\delta} R_{\mathbf{e}_y,\pi} R_{\mathbf{e}_z,\alpha-\delta},$$

for all $\delta \in [0, 2\pi)$, and where $R_{\mathbf{e}_z,\gamma} R_{\mathbf{e}_y,0} R_{\mathbf{e}_z,\alpha}$ and $R_{\mathbf{e}_z,\gamma} R_{\mathbf{e}_y,\pi} R_{\mathbf{e}_z,\alpha}$. We consider a second chart

$$\tilde{R} = R_{\mathbf{e}_x,\tilde{\gamma}} R_{\mathbf{e}_y,\tilde{\beta}} R_{\mathbf{e}_z,\tilde{\alpha}},$$

with $\tilde{\beta} \in (-\pi, \pi]$, $\tilde{\gamma} \in (-\frac{\pi}{2}, \frac{\pi}{2})$, $\tilde{\alpha} \in [0, 2\pi)$, which has ambiguities at $\tilde{\beta} = \pm\frac{\pi}{2}$, cf. [18], see Fig. 13.

The first chart provides a diffeomorphism in an open environment around the ambiguity points of the second chart, and vice versa the second chart provides a diffeomorphism in an open environment of the first chart. A complete atlas of $SE(3)$ is thereby given by

$$(x, y, z, \alpha, \beta, \gamma) \mapsto (x, y, z, R_{\mathbf{e}_z,\gamma} R_{\mathbf{e}_y,\beta} R_{\mathbf{e}_z,\alpha}),$$
$$(x, y, z, \tilde{\alpha}, \tilde{\beta}, \tilde{\gamma}) \mapsto (x, y, z, R_{\mathbf{e}_x,\tilde{\gamma}} R_{\mathbf{e}_y,\tilde{\beta}} R_{\mathbf{e}_z,\tilde{\alpha}})$$

and the corresponding complete atlas of $\mathbb{R}^3 \rtimes S^2$ is given by

$$(x, y, z, \beta, \gamma) \mapsto (x, y, z, [R_{\mathbf{p}}]) \equiv (x, y, z, \cos\gamma \sin\beta, \sin\gamma \sin\beta, \cos\beta),$$
$$(x, y, z, \tilde{\beta}, \tilde{\gamma}) \mapsto (x, y, z, [\tilde{R}_{\mathbf{p}}]) \equiv (x, y, z, \sin\tilde{\beta}, -\cos\tilde{\beta}\sin\tilde{\gamma}, \cos\tilde{\beta}\cos\tilde{\gamma}).$$

The Logarithmic Map

Because $SE(3)$ is a Lie group, the exponential map is linked to the matrix exponentiation of a certain matrix representation for elements of $T_e(SE(3))$. Only the resulting expressions are given here, while the derivations can be found in Duits and Franken [18, Sect. 5.1]. The exponential map of a tangent vector $c^i(\mathbf{x}, Q)A_i$, using the short-hand notation $c^i \equiv c^i(\mathbf{x}, Q)$, is given by

$$\exp(c^i A_i) = \left(\left(I + \tfrac{1-\cos\|\mathbf{c}_2\|}{\|\mathbf{c}_2\|^2}\Omega + \tfrac{1-\operatorname{sinc}\|\mathbf{c}_2\|}{\|\mathbf{c}_2\|^2}\Omega^2\right)\cdot \mathbf{c}_1\ ,\right.$$
$$\left. I + \operatorname{sinc}(\|\mathbf{c}_2\|)\,\Omega + \tfrac{1-\cos\|\mathbf{c}_2\|}{\|\mathbf{c}_2\|^2}\Omega^2\right),$$

where $\mathbf{c}_1 \equiv \mathbf{c}_1(\mathbf{x}, Q) = (c^1, c^2, c^3)^T$ and $\mathbf{c}_2 \equiv \mathbf{c}_2(\mathbf{x}, Q) = (c^4, c^5, c^6)^T$, and with $\Omega \equiv \Omega(\mathbf{x}, Q) = \begin{pmatrix} 0 & -c^6 & c^5 \\ c^6 & 0 & -c^4 \\ -c^5 & c^4 & 0 \end{pmatrix}$. As the exponential map is invertible, the logarithmic map (the inverse of the exponential map) can be derived

$$\log(\mathbf{x}, Q) = \sum_{i=1}^{6} c^i(\mathbf{x}, Q)A_i\,.$$

This equation can be solved to give expressions for c^i in terms of the first chart, resulting in

$$\mathbf{c}_2 = \frac{1}{2\operatorname{sinc}(\tilde{q})}\begin{pmatrix} \sin\beta\,(\sin\alpha - \sin\gamma) \\ \sin\beta\,(\cos\alpha + \cos\gamma) \\ 2\cos^2\frac{\beta}{2}\sin(\alpha+\gamma) \end{pmatrix},$$

where we have $\tilde{q} = \|\mathbf{c}_2\| = \arcsin\sqrt{\cos^2\frac{\alpha+\gamma}{2}\sin^2\beta + \cos^4\frac{\beta}{2}\sin^2(\alpha+\gamma)}$, and

$$\mathbf{c}_1 = \left(I - \frac{1}{2}\Omega + \frac{1}{\tilde{q}^2}\left(1 - \frac{\tilde{q}}{2}\cot\frac{\tilde{q}}{2}\right)\Omega^2\right)\cdot\mathbf{x}.$$

This last expression is retained when rewriting the logarithmic map in terms of the second chart, but for $\tilde{q}$ and $\mathbf{c}_2$ we have

$$\tilde{q} = \arcsin\sqrt{\cos^4\tfrac{\tilde{\gamma}}{2}\sin^2\tilde{\beta} + \cos^2\tfrac{\tilde{\beta}}{2}\sin^2\tilde{\gamma}},$$

$$\mathbf{c}_2 = \tfrac{1}{\operatorname{sinc}(\tilde{q})}\begin{pmatrix} \sin\tilde{\gamma}\cos^2\frac{\tilde{\beta}}{2} \\ \sin\tilde{\beta}\cos^2\frac{\tilde{\gamma}}{2} \\ \frac{1}{2}\sin\tilde{\gamma}\sin\tilde{\beta} \end{pmatrix}.$$

Finite Difference Schemes

The finite difference stencils used in the Mathematica package are given here. Writing $Q_{\mathbf{v},\alpha}$ for a rotation by angle α around $\mathbf{v}$ expressed in the second coordinate chart, we find the explicit formulas for the vector fields on $\mathbb{R}^3 \rtimes S^2$ given below. h_s and h_a are respectively the spatial and angular step sizes. h_s is typically 0.88, see Creusen [12], while h_a depends on the distribution of sample points on the sphere. See Duits and Franken [18, Chap. 7] for the derivation of these formulas from Eq. (10).

Remark 8. The use of single values for h_s and h_a relies on approximately equidistantly sampled data.

The three different finite differences schemes considered are given below. Second order derivatives are calculated by repeating the listed first order derivatives.

Central derivatives

$$\begin{aligned}
\mathscr{A}_1 U(\mathbf{x},\mathbf{n}) &\approx \frac{U(\mathbf{x}+h_s Q_{\mathbf{n}}\mathbf{e}_x,\mathbf{n})-U(\mathbf{x}-h_s Q_{\mathbf{n}}\mathbf{e}_x,\mathbf{n})}{2h_s}\\
\mathscr{A}_2 U(\mathbf{x},\mathbf{n}) &\approx \frac{U(\mathbf{x}+h_s Q_{\mathbf{n}}\mathbf{e}_y,\mathbf{n})-U(\mathbf{x}-h_s Q_{\mathbf{n}}\mathbf{e}_y,\mathbf{n})}{2h_s}\\
\mathscr{A}_3 U(\mathbf{x},\mathbf{n}) &\approx \frac{U(\mathbf{x}+h_s Q_{\mathbf{n}}\mathbf{e}_z,\mathbf{n})-U(\mathbf{x}-h_s Q_{\mathbf{n}}\mathbf{e}_z,\mathbf{n})}{2h_s}\\
\mathscr{A}_4 U(\mathbf{x},\mathbf{n}) &\approx \frac{U(\mathbf{x},Q_{\mathbf{n}}Q_{\mathbf{e}_x,h_a}\mathbf{e}_z)-U(\mathbf{x},Q_{\mathbf{n}}Q_{\mathbf{e}_x,-h_a}\mathbf{e}_z)}{2h_a}\\
\mathscr{A}_5 U(\mathbf{x},\mathbf{n}) &\approx \frac{U(\mathbf{x},Q_{\mathbf{n}}Q_{\mathbf{e}_y,h_a}\mathbf{e}_z)-U(\mathbf{x},Q_{\mathbf{n}}Q_{\mathbf{e}_y,-h_a}\mathbf{e}_z)}{2h_a}
\end{aligned}$$

Forward derivatives

$$\begin{aligned}
\mathscr{A}_1 U(\mathbf{x},\mathbf{n}) &\approx \frac{U(\mathbf{x}+h_s Q_{\mathbf{n}}\mathbf{e}_x,\mathbf{n})-U(\mathbf{x},\mathbf{n})}{h_s}\\
\mathscr{A}_2 U(\mathbf{x},\mathbf{n}) &\approx \frac{U(\mathbf{x}+h_s Q_{\mathbf{n}}\mathbf{e}_y,\mathbf{n})-U(\mathbf{x},\mathbf{n})}{h_s}\\
\mathscr{A}_3 U(\mathbf{x},\mathbf{n}) &\approx \frac{U(\mathbf{x}+h_s Q_{\mathbf{n}}\mathbf{e}_z,\mathbf{n})-U(\mathbf{x},\mathbf{n})}{h_s}
\end{aligned}$$

Backward derivatives

$$\begin{aligned}
\mathscr{A}_1 U(\mathbf{x},\mathbf{n}) &\approx \frac{U(\mathbf{x},\mathbf{n})-U(\mathbf{x}-h_s Q_{\mathbf{n}}\mathbf{e}_x,\mathbf{n})}{h_s}\\
\mathscr{A}_2 U(\mathbf{x},\mathbf{n}) &\approx \frac{U(\mathbf{x},\mathbf{n})-U(\mathbf{x}-h_s Q_{\mathbf{n}}\mathbf{e}_y,\mathbf{n})}{h_s}\\
\mathscr{A}_3 U(\mathbf{x},\mathbf{n}) &\approx \frac{U(\mathbf{x},\mathbf{n})-U(\mathbf{x}-h_s Q_{\mathbf{n}}\mathbf{e}_z,\mathbf{n})}{h_s}
\end{aligned}$$

For the spatial derivatives, a simplified version of the upwind biased scheme is implemented in order to properly handle boundary effects. The scheme first calculates the central derivative in every point. Then for every point, depending on the sign of the central derivative, either the forward- or the backward derivative is calculated. A positive value of the central derivative means a backward derivative is calculated. The ensemble of forward- and backward derivatives in all points is then the actual derivative. The angular derivatives are all calculated using central derivatives.

Acknowledgements The authors are grateful to the Kempenhaeghe Epilepsy Center, who supplied the MRI data. Furthermore, the authors would like to thank the anonymous reviewers for their helpful comments, and the editors for their work in making this publication happen.

References

1. Aganj, I., Lenglet, C., Jahanshad, N., Yacoub, E., Harel, N., Thompson, P., Sapiro, G.: A hough transform global probabilistic approach to multiple-subject diffusion MRI tractography. Med. Image Anal. **15**(4), 414–425 (2011)
2. Alexander, D., Barker, G., Arridge, S.: Detection and modeling of non-Gaussian apparent diffusion coefficient profiles in human brain data. Magn. Reson. Med. **48**(2), 331–340 (2002)
3. Aubin, T.: A Course in Differential Geometry. American Mathematical Society, Providence (2001)
4. Basser, P., Mattiello, J., Le Bihan, D.: MR diffusion tensor spectroscopy and imaging. Biophys. J. **66**, 259–267 (1994)
5. Bellaïche, B.: The tangent space in sub-Riemannian geometry. J. Math. Sci. **83**(4), 461–476 (1996)
6. Burgeth, B., Weickert, J.: An explanation for the logarithmic connection between linear and morphological systems. In: Proceedings of the 4th International Conference, Scale Space 2003, Isle of Skye, pp. 325–339. Springer (2003)
7. Burgeth, B., Breuß, M., Pizarro, L., Weickert, J.: PDE-driven adaptive morphology for matrix fields. In: Scale Space and Variational Methods in Computer Vision, Voss, pp. 247–258 (2009)
8. Burgeth, B., Didas, S., Weickert, J.: A general structure tensor concept and coherence-enhancing diffusion filtering for matrix fields. In: Laidlaw, D., Weickert, J. (eds.) Visualization and Processing of Tensor Fields: Advances and Perspectives, pp. 305–324. Springer, Berlin (2009)
9. Burgeth, B., Pizarro, L., Didas, S.: Edge-enhancing diffusion filtering for matrix fields. In: Laidlaw, D.H., Vilanova, A. (eds.) New Developments in the Visualization and Processing of Tensor Fields, pp. 51–67. Springer, Berlin/Heidelberg (2012)
10. Chirikjian, G., Kyatkin, A.: Engineering Applications of Noncommutative Harmonic Analysis: With Emphasis on Rotation and Motion Groups. CRC, Boca Raton (2000)
11. Crandall, M.G., Lions, P.L.: Viscosity solutions of Hamilton-Jacobi equations. Trans. Am. Math. Soc. **277**(1), 1–42 (1983)
12. Creusen, E.: Numerical schemes for linear and non-linear enhancement of HARDI data. Master's thesis, Eindhoven University of Tecnhology (2010)
13. Creusen, E., Duits, R., Dela Haije, T.: Numerical schemes for linear and non-linear enhancement of HARDI data. In: Proceedings of the Third International Conference on Scale Space and Variational Methods in Computer Vision, Ein-Gedi. Lecture Notes in Computer Science, vol. 12 (2011)
14. Creusen, E., Duits, R., Vilanova, A., Florack, L.: Numerical schemes for linear and non-linear enhancement of DW-MRI. Numer. Math.: Theory Methods Appl. **6**, 138–168 (2013)
15. Dela Haije, T.: Geometrical methods for enhancement and tractography in diffusion MRI. Master's thesis, Eindhoven University of Technology (2012)
16. Descoteaux, M., Angelino, E., Fitzgibbons, S., Deriche, R.: Regularized, fast, and robust analytical Q-ball imaging. Magn. Reson. Med. **58**(3), 497–510 (2007)
17. Duits, R.: Perceptual organization in image analysis. Ph.D. thesis, Technische Universiteit Eindhoven (2005)
18. Duits, R., Franken, E.: Left-invariant diffusions on the space of positions and orientations and their application to crossing-preserving smoothing of HARDI images. Int. J. Comput. Vis. **92**(3), 231–264 (2011)

19. Duits, R., Creusen, E., Ghosh, A., Dela Haije, T.: Diffusion, convection and erosion on $\mathbb{R}^3 \rtimes S^2$ and their application to the enhancement of crossing fibers. CASA report 18, Technische Universiteit Eindhoven (2011). http://arxiv.org/abs/1103.0656v5
20. Duits, R., Dela Haije, T., Creusen, E., Ghosh, A.: Morphological and linear scale spaces for fiber enhancement in DW-MRI (2012, to appear). J. Math. Imaging Vis. http://link.springer.com/article/10.1007%2Fs10851-012-0387-2
21. Duits, R., Dela Haije, T.C.J., Ghosh, A., Creusen, E.J., Vilanova, A., ter Haar Romeny, B.: Fiber enhancement in diffusion-weighted MRI. In: Scale Space and Variational Methods in Computer Vision. Lecture Notes in Computer Science, vol. 6667 (Springer, Berlin/Heidelberg, 2012), pp. 1–13
22. Dungey, N., ter Elst, A.F.M., Robinson, D.W.: Analysis on Lie Groups with Polynomial Growth. Progress in Mathematics, vol. 214. Birkhäuser, Boston (2003)
23. Efron, B., Tibshirani, R.J.: An Introduction to the Bootstrap. Monographs on Statistics and Applied Probability, vol. 57. Chapman & Hall, New York (1997)
24. Evans, L.: Partial Differential Equations. Graduate Studies in Mathematics, vol. 19. American Mathematical Society, Providence (1998)
25. Florack, L.: Codomain scale space and regularization for high angular resolution diffusion imaging. In: Aja Fernández, S., de Luis Garcia, R. (eds.) CVPR Workshop on Tensors in Image Processing and Computer Vision, Anchorage (2008)
26. Florack, L., Balmachnova-Sizykh, E.: Decomposition of high angular resolution diffusion images into a sum of self-similar polynomials on the sphere. In: Proceedings of the 18th International Conference on Computer Graphics and Vision, Moscow, pp. 26–31 (2008)
27. Franken, E.: Enhancement of crossing elongated stuctures in images. Ph.D. thesis, Technische Universiteit Eindhoven (2008)
28. Hagmann, P., Jonasson, L., Maeder, P., Thiran, J.P., Wedeen, V., Meuli, R.: Understanding diffusion MR imaging techniques: from scalar diffusion-weighted imaging to diffusion tensor imaging and beyond. Radiographics **26**, S205–S223 (2006)
29. Hess, C.P., Mukherjee, P., Tan, E.T., Xu, D., Vigneron, D.B.: Q-ball reconstruction of multimodal fiber orientations using the spherical harmonic basis. Magn. Reson. Med. **56**, 104–117 (2006)
30. Hörmander, L.: Hypoelliptic second order differential equations. Acta Math. **119**(1), 147–171 (1967)
31. Jackway, P.: Morphological scale-space. In: Proceedings 11th IAPR International Conference on Pattern Recognition, The Hague, pp. 252–255. Society Press (1992)
32. Jeurissen, B., Leemans, A., Jones, D., Tournier, J.D., Sijbers, J.: Probabilistic fiber tracking using the residual bootstrap with constrained spherical deconvolution. Hum. Brain Mapp. **32**, 461–479 (2011)
33. Jones, D., Cercignani, M.: Twenty-five pitfalls in the analysis of diffusion MRI data. NMR Biomed. **23**, 803–820 (2010)
34. Le Bihan, D., Breton, E., Lallemand, D., Grenier, P., Cabanis, E., Laval-Jeantet, M.: MR imaging of intravoxel incoherent motions: application to diffusion and perfusion in neurologic disorders. Radiology **601**(2), 401–407 (1986)
35. Manfredi, J., Stroffolini, B.: A version of the Hopf-Lax formula in the Heisenberg group. Commun. Partial Differ. Equ. **27**(5), 1139–1159 (2002)
36. Moseley, M., Cohen, Y., Kucharchzyk, J., Mintorovitch, J., Asgari, H., Wendland, M., Tsuruda, J., Norman, D.: Diffusion-weighed MR imaging of anisotropic water diffusion in cat nervous system. Radiology **176**(2), 439–445 (1990)
37. Nagel, A., Ricci, F., Stein, E.: Fundamental solutions and harmonic analysis on nilpotent groups. Bull. Am. Math. Soc. **23**(1), 139–144 (1990)
38. Özarslan, E., Mareci, T.: Generalized diffusion tensor imaging and analytical relationships between diffusion tensor imaging and high angular resolution imaging. Magn. Reson. Med. **50**, 955–965 (2003)
39. Özarslan, E., Shepherd, T., Vemuri, B., Blackband, S., Mareci, T.: Resolution of complex tissue microarchitecture using the diffusion orientation transform (DOT). NeuroImage **31**, 1086–1103 (2006)

40. Pizarro, L., Burgeth, B., Didas, S., Weickert, J.: A generic neighbourhood filtering framework for matrix fields. In: Computer Vision-ECCV 2008, Marseille, pp. 521–532. Springer (2008)
41. Prčkovska, V., Rodrigues, P., Duits, R., ter Haar Romeny, B., Vilanova, A.: Extrapolating fiber crossings from DTI data: can we gain the same information as HARDI? Technical report, Technische Universiteit Eindhoven (2010)
42. Reisert, M., Skibbe, H.: Left-invariant diffusion on the motion group in terms of the irreducible representations of SO(3). http://arxiv.org/pdf/1202.5414v1.pdf
43. Rodrigues, P., Duits, R., Vilanova, A., ter Haar Romeny, B.: Accelerated diffusion operators for enhancing DW-MRI. In: Bartz, D., Botha, C., Hornegger, J., Machiraju, R. (eds.) Eurographics Workshop on Visual Computing for Biology and Medicine, Leipzig, pp. 49–56 (2010)
44. Roerdink, J.: Group morphology. Pattern Recognit. **33**, 877–895 (2000)
45. Sherbondy, A., Doughery, R., Ben-Shachar, M., Napel, S., Wandell, B.: ConTrack: finding the most likely pathways between brain regions using diffusion tractography. J. Vis. **8**(15), 1–16 (2008)
46. Stejskal, E., Tanner, J.: Spin diffusion measurements: spin echoes in the presence of a time-dependent field gradient. J. Chem. Phys. **43**, 288–293 (1965)
47. Tabelow, K., Polzehl, J., Spokoiny, V., Voss, H.: Diffusion tensor imaging: structural adaptive smoothing. NeuroImage **39**(4), 1763–1773 (2008)
48. Tabelow, K., Keller, S., Mohammadi, S., Kugel, H., Gerdes, J., Polzehl, J., Deppe, M.: Structural adaptive smoothing increases sensitivity of DTI to detect microstructure alterations. In: Poster at the 17th Annual Meeting of the Organization for Human Brain Mapping, Québec City (2011)
49. Tax, C., Duits, R., Vilanova, A., ter Haar Romeny, B., Leemans, A., Ossenblok, P.: Evaluating contextual processing in diffusion MRI: application to optic radiation reconstruction for epilepsy surgery (2012). To Apear on arXiv July 2012
50. van den Boomgaard, R., Smeulders, A.: The morphological structure of images: the differential equations of morphological scale-space. IEEE Trans. Pattern Anal. Mach. Intell. **16**(11), 1101–1113 (1994)
51. Warach, S., Chien, D., Li, W., Ronthal, M., Edelman, R.: Fast magnetic resonance diffusion-weighted imaging of acute human stroke. NeuroImage **42**(9), 1717–1723 (1992)
52. Wedeen, V., Hagmann, P., Tseng, W., Reese, T., Weiskoff, R.: Mapping complex tissue architecture with diffusion spectrum magnetic resonance imaging. Magn. Reson. Med. **54**(6), 1377–1386 (2005)
53. Welk, M.: Families of generalised morphological scale spaces. In: Scale Space Methods in Computer Vision, Isle of Skye. Lecture Notes in Computer Science, pp. 770–784 (2003)